ACS OMEGA

http://pubs.acs.org/journal/acsodf

Article

Scalable Synthesis of Few-Layered 2D Tungsten Diselenide (2H-WSe_2) Nanosheets Directly Grown on Tungsten (W) Foil Using Ambient-Pressure Chemical Vapor Deposition for Reversible Li-Ion Storage

Rajashree Konar, Rosy, Ilana Perelshtein, Eti Teblum, Madina Telkhozhayeva, Maria Tkachev, Jonathan J. Richter, Elti Cattaruzza, Andrea Pietropolli Charmet, Paolo Stoppa, Malachi Noked,* and Gilbert Daniel Nessim*

Cite This: *ACS Omega* 2020, 5, 19409−19421

Read Online

ACCESS | Metrics & More | Article Recommendations | Supporting Information

ABSTRACT: We report a facile two-furnace APCVD synthesis of 2H-WSe_2. A systematic study of the process parameters is performed to show the formation of the phase-pure material. Extensive characterization of the bulk and exfoliated material confirm that 2H-WSe_2 is layered (i.e., 2D). X-ray diffraction (XRD) confirms the phase, while high-resolution scanning electron microscopy (HRSEM), high-resolution transmission electron microscopy (HRTEM), and atomic force microscopy (AFM) clarify the morphology of the material. Focused ion beam scanning electron microscopy (FIB-SEM) estimates the depth of the 2H-WSe_2 formed on W foil to be around 5−8 μm, and Raman/UV−vis measurements prove the quality of the exfoliated 2H-WSe_2. Studies on the redox processes of lithium-ion batteries (LiBs) show an increase in capacity up to 500 cycles. On prolonged cycling, the discharge capacity up to the 50th cycle at 250 mA/g of the material shows a stable value of 550 mAh/g. These observations indicate that exfoliated 2H-WSe_2 has promising applications as an LiB electrode material.

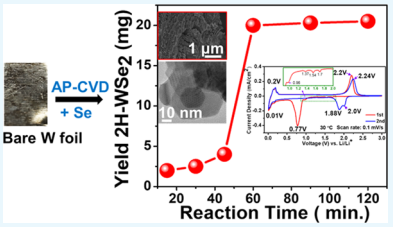

INTRODUCTION

As the demand for sustainable energy storage devices increases, we require new materials for energy storage systems that will alleviate the cost and increase their longevity. A worthwhile and prominent energy storage technology for modern applications is the development of lithium-ion batteries. These batteries are currently used in electric vehicles, portable electronics, etc. and have become a part of our daily life.[1−3] In this regard, two-dimensional (2D) materials have also attracted substantial and considerable attention due to their unique properties and abundant potential in various applications, including batteries.[4−6] A controllable synthesis of 2D materials with high quality and high efficiency is essential for their large-scale applications, for instance, their functions as electrode material in batteries.[7] There are many methods for the synthesis of two-dimensional materials, including mechanical exfoliation,[8] liquid exfoliation,[9] liquid-phase routes,[1,10] and chemical vapor deposition (CVD).[11,12] Among these processes, CVD offers better quality, efficiency, consistency, and control over the others.[13] The efficiency of CVD-assisted synthesis is quite higher compared to mechanical exfoliation, and the quality control is better than liquid-phase routes, due to which CVD has been recognized as a reliable route for preparing high-quality two-dimensional (2D) materials.[11] In this perspective, the family of 2D transition-metal dichalcogenides (TMDCs) gained significant attention due to their ability to store metal ions such as Li, Na, and Mg.[14,15] The behaviors of 2D TMDCs are varied, ranging from insulating, semiconducting, and metallic to superconducting.[16] TMDCs of group 6 transition metals (MX_2 where M = Mo, W, and X = S, Se, Te) have a lamellar structure (space group *P*63/*mmc*) similar to graphite but with larger interlayer spacing.[12] Here, in this 2D family, tungsten dichalcogenides are significant because of the larger size of W, which provides a further alteration of the 2D structure.[17] Although WO_3 and WS_2 are still the popular members of this TMDC subfamily in various applications, tungsten diselenide (WSe_2) is among the emerging candidates in the family of TMDC and is successfully utilized for various applications such as in photodetectors,[18] field-effect transistors (FETs),[19] etc. It has a typical group 6 TMDC lattice structure, where W atoms are confined in a trigonal prismatic coordination sphere near Se atoms.[12] WSe_2 has a layered crystal structure similar to WS_2. The latter (i.e., WS_2) is also extensively studied as a possible anode material

Received: March 16, 2020
Accepted: July 13, 2020
Published: July 24, 2020

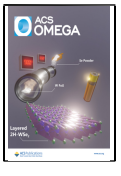

for LiBs,[20] and the reaction mechanism of WSe_2 in LiB application is also found to be similar to that of WS_2.[19] WSe_2 possesses unique properties such small band gap (1.6 eV) and large adjacent layer spacing (0.648 nm, 2 times larger than that of graphite), which can effectively facilitate reversible ion intercalation and extraction. Because of its very high density of 9.32 g cm^{-3}, WSe_2 also has a high volumetric capacity, and these properties help manifest this material as a prospective electrode material.[21−24]

Usually, the synthesis methods for TMDCs using CVD is either a top-down or a bottom-up approach.[25] CVD-assisted processes include precursors that are reacted and/or decomposed and deposited as a monolayer or few-layered thin films on appropriate substrates such as sapphire, Si/SiO_2, etc. The four common routes of synthesis can be summarized based on (1) thermal decomposition of precursors, (2) selenization of predeposited metal or metal oxide films on suitable substrates, (3) physical vapor transport between presynthesized TMDC and an insulating substrate, or (4) vapor-phase reaction between two precursors (i.e., the transition-metal oxide/halide and chalcogen precursor).[26] The vapor-phase reaction of the CVD process is classified into atmospheric pressure CVD (APCVD),[27,28] modified metal−organic CVD (m-MOCVD),[29,30] and low-pressure CVD (LPCVD).[31,32] Our method of synthesis combines the synthetic routes mentioned in (3) and (4), which helps us to report a facile and scalable two-furnace bulk synthesis of tungsten diselenide (WSe_2) on tungsten (W) foil using only elemental selenium (Se) powder as a precursor, using an atmospheric pressure chemical vapor deposition system (APCVD). Several reports of WSe_2 thin-film growth by CVD on different substrates are reported, but using different precursors, such as WF_6, H_2Se, $W(CO)_6$, $SeCl_4$, etc.,[33] as the starting materials, which are often tricky to handle involving burdensome processes. For example, using H_2S or H_2Se as the chalcogen precursor or involving an intermediate process of annealing the substrate with Ar/H_2 or using chalcogen precursors such as thiourea in solvothermal methods gives rise to problems in handling these gases as a byproduct of the reaction because they are hazardous to human health.[34,35]

In this article, we report a facile synthesis of 2H-WSe_2 on W foil in an ambient-pressure chemical vapor deposition (APCVD) system using only argon as a carrier gas without the formation of any hazardous waste products during the reaction. The idea behind the preparation of this material using APCVD is (1) to show that synthesis of transition-metal dichalcogenides with a higher melting point of the metal is possible using a two-furnace system in the absence of high pressure and continuous heating at higher temperatures for days, thereby simplifying our procedure for this synthesis, (2) to study the possible growth route of 2H-WSe_2 formation on W foil for exploring how this material can be easily exfoliated and integrated into a possible electrode material for lithium-ion batteries, (3) to estimate the maximum yield obtained from liquid-phase exfoliations of the 2H-WSe_2 grown on the W foil, and (4) to observe if a single-step reaction was feasible in producing phase-pure material on the exposed surface of W foil. Since the bulk material was exfoliated to prepare the electrodes, we also investigated if the yield from the reactions was increased as a function of reaction time. Conventional LiB electrodes are usually composed of materials often synthesized using hydrothermal or solvothermal procedures with specific morphologies (such as spheres) in favor of the performance of the material in LiB.[36−38] Since, among the TMDCs, 2H-WSe_2 synthesized in APCVD has a platelike morphology, we decided to inspect it as a possible electrode material for battery application because there are very few reports on the ability of exfoliated 2H-WSe_2 to function as a lithium-ion battery electrode.

RESULTS AND DISCUSSION

To the best of our knowledge, a phase diagram for W and Se is not available in the literature. Therefore, to understand the possible reactions between Se and W precursors, as a function of temperature and pressure, we relied on previous reports of this material. It is reported that 2H-WSe_2 can be synthesized using traditional solid-state mixing of WO_3 powder with elemental Se, sealing them in quartz ampoules, and heating at ca. 700−800 °C for a few days in an inert atmosphere. The final product is usually crushed or ground to obtain flakes of layered WSe_2.[39] Other methods of preparation include surface selenization of tungsten (W) or tungsten oxide (WO_3) thin films,[40] using magnetron sputtering,[41] molecular beam epitaxy,[40,42] etc., but, in our experiments, we found out that the reaction between the tungsten foil and the elemental selenium takes place (in the absence of pressure) at 900 °C (indicating the reaction did not occur between 600 and 850 °C) in F2 while heating the elemental Se precursor at 650 °C in F1. (The schematic of the furnace system is shown in Figure 1). This temperature gradient of 250 °C between the two

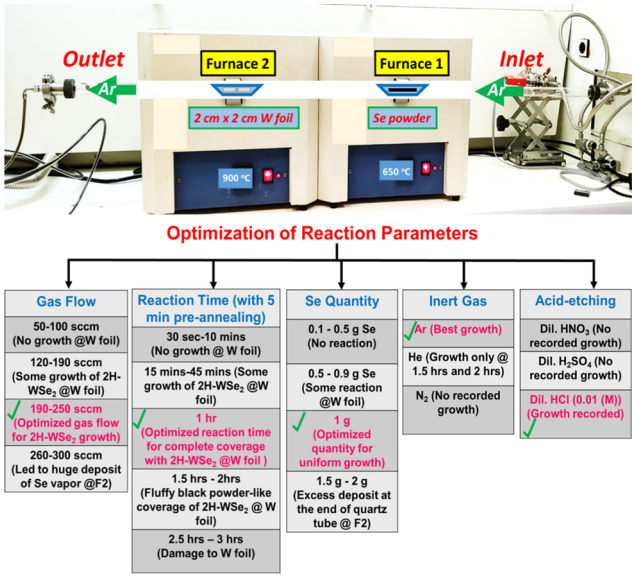

Figure 1. Photo of the APCVD system used with a schematic of the growth of 2H-WSe_2 in a two-furnace CVD system and a summary of optimization of reaction parameters. (Photograph was taken by Rajashree Konar, Copyright 2020).

furnaces is vital to maintain throughout the reaction time because it allows the vapor from the elemental Se to react and deposit on the surface of the W metal foil. The Se boat was immediately pulled out once the reaction was over, and the WSe_2 sample was allowed to cool gradually to room temperature. For optimizing the mentioned reaction, we tested the effect of several reaction parameters, which we summarize as follows:

https://dx.doi.org/10.1021/acsomega.0c01155
ACS Omega 2020, 5, 19409−19421

(1) Optimization of carrier gas flow: To study the dependency of the WSe_2-film growth on the flow rates of the carrier gas (argon in this case), the Ar flow rate was varied from 50 to 300 sccm during the reaction. It was observed that at lower Ar flow rates (i.e., from 50 to 100 sccm), no growth was observed at 900 °C. Higher flow rates, starting from 150 sccm onward, resulted in a substantial growth of WSe_2. The reaction conditions were finally optimized at 200 sccm because the growth of WSe_2 was found to be the most uniform with this Ar flow. Further increase in the flow rate to 250 and 300 sccm did not lead to any significant reaction between the W foil and the elemental Se precursor because a significant amount of selenium vapor was found to be condensed at the end of the quartz tube outside the furnace F2.

(2) Optimization of reaction time: Different reaction times from 30 s to 3 h were investigated to achieve efficient synthesis protocol. Initial results of X-ray diffraction (XRD) and high-resolution scanning electron microscopy (HRSEM) indicated that the reaction did not occur for reaction times shorter than 15 min, from which we can assume that the minimum time to drive this reaction is 15 min in configuration. Reactive annealing did not result in uniform coverage of the W foil with WSe_2, so we preannealed the W foil in the inert atmosphere before introducing the elemental Se vapor from furnace F1. We observed that a preannealing step of 5 min was the best for 2H-WSe_2 growth on W foil. Longer reaction times between the acid-etched W foil and elemental Se from 2.5 h up to 3 h led to bending of the foil itself and failed to provide us with any critical data. The optimized reaction time in our case is 1 h between W foil and Se. We also tried to understand the physical changes associated with the synthesis of this material. Since the reaction occurred mainly between the W foil and the elemental selenium, we varied the reaction times between them, ranging from 1 min up to 2 h. We observed for the reaction times of 1, 5, and 10 min that there was no growth of WSe_2 on the surface. For reaction times of 15 min and above, we observed a thin grayish coating on the top of the W foil. At longer reaction times of 30 min, 45 min, and 1 h, we observed a significant growth of WSe_2, as indicated by the subtle changes in the color (which was becoming relatively darker) of the exposed surface of the W foil. But at further reaction times of 2 and 3 h, there were no significant visual changes, and these were observed according to the high-resolution scanning electron microscopy (HRSEM) images (although we could not image or analyze the material formed at 3 h because it was stuck to the boat and got damaged).

(3) Optimization of Se precursor quantity: The dependency of WSe_2-film growth on the amount of elemental selenium was also investigated by varying the precursor quantity in the range of 0.1−2 g. No significant reaction was observed for loadings of less than 1 g. However, when the Se quantity was 0.5−0.9 g, deposits of unreacted Se were found adsorbed on the W foil. For Se loadings greater than 1 g (1.5 and 2 g), a black deposit of excess Se vapor was observed along with the 2H-WSe_2 at the end of the quartz tube. Consequently, 1 g of elemental Se powder was found to be the optimized loading and was used throughout for the synthesis of 2H-WSe_2.

(4) Optimization of inert carrier gas: The role of the inert atmosphere during the synthesis was also carefully investigated. The study was carried out using three different inert carrier gases: nitrogen (N_2), helium (He), and argon (Ar). The results showed that there was no reaction in a nitrogen atmosphere. Helium atmosphere showed some growth (only at longer reaction times of 1.5 and 2 h between W foil and elemental Se (Supporting Figure S1)), but the yield and the coverage of the foil with WSe_2 were very low. Only argon showed significant growth and yield compared to a helium atmosphere at specified reaction times.

(5) Effect of acid etching: All of the aforementioned reaction conditions were implemented for two sets of W foils. One was cleaned with 0.01 (M) HCl and isopropanol before the reaction, while the other was cleaned only with isopropanol and used in the as-purchased condition. We observed that the acid-etched W foil exhibited much better growth in comparison to the unetched W foil. The growth observed on the unetched W foil was nonconformal, similar to the growth patterns observed in the acid-etched W foil (reacting with Se at 15 min reaction time) but only at longer reaction times (1.5 and 2 h). This indicated that the nucleation sites occurring due to acid etching, as well as the removal of native oxide from W foil surface, helped in the formation of 2H-WSe_2 sheets on the W foil.

We also conducted a postannealing of the as-grown WSe_2 at 900 °C in argon after the selenization reaction was completed. This resulted in (i) more substantial grain growth of the as-grown WSe_2 as well as (ii) significant damage to the W foil itself (on prolonged heating), which was stuck to the quartz boat, being ineffective and too much degraded for further analyses.

Several researchers have found that hydrogen plays a vital role in the growth of TMDCs. It acts as an additional reducing agent with Se during the growth of nanosheets and thin films when elemental Se and metal oxides are used as precursors.[7] But in our case, the absence of H_2 as a reducing agent simplified our synthetic procedure and dismissed the possibility of having H_2Se (very toxic gas) as a byproduct. It also indicated that the synthesis could take place only with a simply diluted acid etching (taking 0.01 (M) of HCl) of the W foil before selenization. Keeping in mind the above reaction parameters, we have summarized the optimization process, as shown in Figure 1. The optimized reaction was also employed to a larger set of W foils (having cross section 4 cm × 4 cm with the same thickness of 0.127 mm), and we observed that this process could be scaled up easily.

The X-ray diffractogram analysis of tungsten diselenide in an argon atmosphere synthesized at 1 h reaction time between W foil and Se in Figure 2 indicated that a phase-pure material of high crystallinity was synthesized with a hexagonal crystal system of space group *P*63/*mmc* and space group no. 194, where all of the diffraction peaks could be indexed to the ICDD no: 00-038-1388 of 2H-WSe_2, according to the literature. The peaks of both bulk and exfoliated 2H-WSe_2 were compared, and it showed that there were changes in the intensities of the (002) peak at 13.6° and the (105) peak at 47.5°. The diffractograms also indicated a slight left shift for

https://dx.doi.org/10.1021/acsomega.0c01155
ACS Omega 2020, 5, 19409−19421

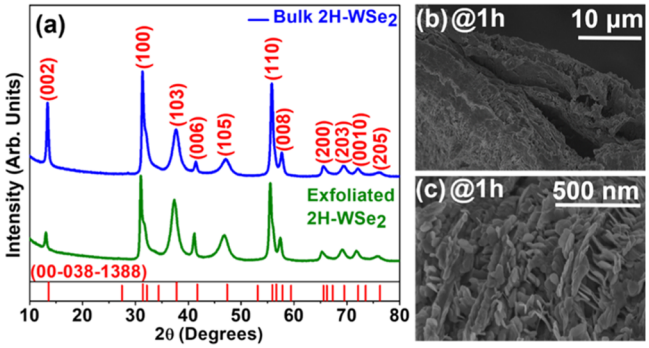

Figure 2. (a) XRD pattern of bulk and exfoliated tungsten diselenide (WSe_2) for comparison with the reported ICDD no. of 2H-WSe_2 obtained for 1 h reaction between tungsten foil and elemental selenium. (b, c) Low-magnification and high-magnification HRSEM images of 2H-WSe_2 at 1 h reaction between W foil and elemental Se.

the exfoliated 2H-WSe_2 in comparison to the bulk 2H-WSe_2. The peaks could be assigned as follows for each: (100), (103), (006), (105), (008), (107), (108), (203), (0010), and (205) at around 31.4, 37.8, 41.7, 47.3, 56.6, 59.4, 66.2, 69.4, 72.7, and 76.2° respectively. The analysis of the XRD data also showed an interesting detail regarding our material. The area of each peak is different, signifying that there is anisotropic broadening in the XRD pattern of the material. Such an anomaly can be expected because WSe_2 has a crystal structure in which the atoms are connected by covalent bonds along the in-plane direction. In contrast, the atoms interacted via van der Waals forces along the through-plane direction.[41,43] Therefore, the different interactions and bond strengths, as well as the particle size, can lead to different distortions along different planes of growth, which is observed in the X-ray diffractogram in our case. Also, it must be noted that, in general, peak broadening in X-ray diffraction measurements also indicates the formation of nanometer-sized sheets. This signifies that the material also contains both micron- and nanosized sheets. It can happen due to several reasons, the prominent one being the agglomeration of the nanosized sheets into a larger mass, which ultimately breaks up into individual sheets following the ultrasonic liquid-assisted exfoliation. From the comparison of the XRD pattern between the bulk and the exfoliated 2H-WSe_2, the intensity of the (002) peak seems to decrease, while the intensities of the (100), (103), (105), and (0010) peaks seem to show an increasing trend. So, we can conclude from the XRD measurements that 2H-WSe_2 shows a particular orientation of growth along the aforementioned planes. In addition to analyzing both the bulk and exfoliated materials, we also checked for free peaks of metallic tungsten and elemental selenium in both cases and observed that there was none. This indicated that the samples we synthesized were of high purity, and no unreacted W or Se was present. The investigation of the nanosheet size was established further using high-resolution scanning electron microscopy (HRSEM) and transmission electron microscopy (TEM) characterizations. The high-magnification HRSEM image of the nanosheets is shown in Figure 2c.

From the HRSEM and HRTEM images, we observed that the material synthesized at 1 h reaction time (i.e., optimized reaction time) exhibited both bigger and smaller flakes/sheets. The smaller sheets were around 50 nm, and the larger sheets were around 80 nm in length (Supporting Figure S2). From previous reports, it is understood that CVD-assisted syntheses tend to lead to the formation of the thermodynamically stable phase, i.e., 2H-WSe_2. In our case, we obtained the same results and reproducibility from all XRD and HRSEM imaging data at different reaction times. Based on this, we hypothesize the following: the bare unetched as well as etched W foils were unreactive at short reaction times of 1, 5, and 10 min. This indicates that the surface roughness of the W foil was a significant indicator of growth. But since the reaction occurred from 15 min onward, we can assume that both thermal annealing and a longer exposure time of the etched W foil to Se led to a reaction on the surface of the W foil. This was also according to the HRSEM images in Figure 3a–f, indicating

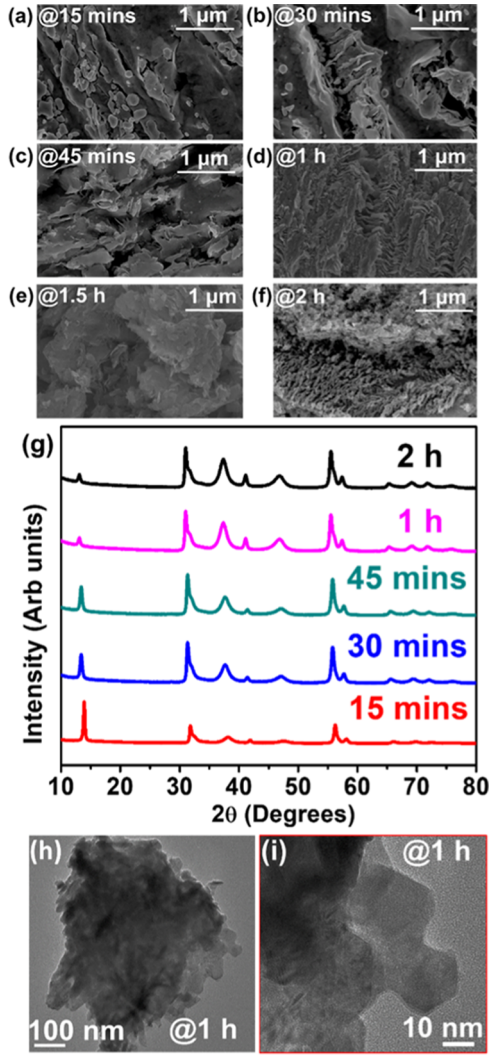

Figure 3. Microstructural evolution of 2H-WSe_2 on W foil at (a) 15 min, (b) 30 min, (c) 45 min, (d) 1 h, (e) 1.5 h, and (f) 2 h; (g) XRD pattern of 2H-WSe_2 with respect to time variation; and (h, i) bright-field (BF)-TEM images of 2H-WSe_2 synthesized at 1 h reaction time.

that the bulk material had layered growth on it, and it was consistent throughout the surface of the W foil. A closer inspection at higher magnifications of the exfoliated material sheds light on the shape of the nanosheets, which were stacked on top of each other.

The observations above prompted us to present a possible reaction mechanism for the formation of 2H-WSe_2 on W foil, with the reaction scheme shown in Figure 4. The bare W foil

https://dx.doi.org/10.1021/acsomega.0c01155
ACS Omega 2020, 5, 19409−19421

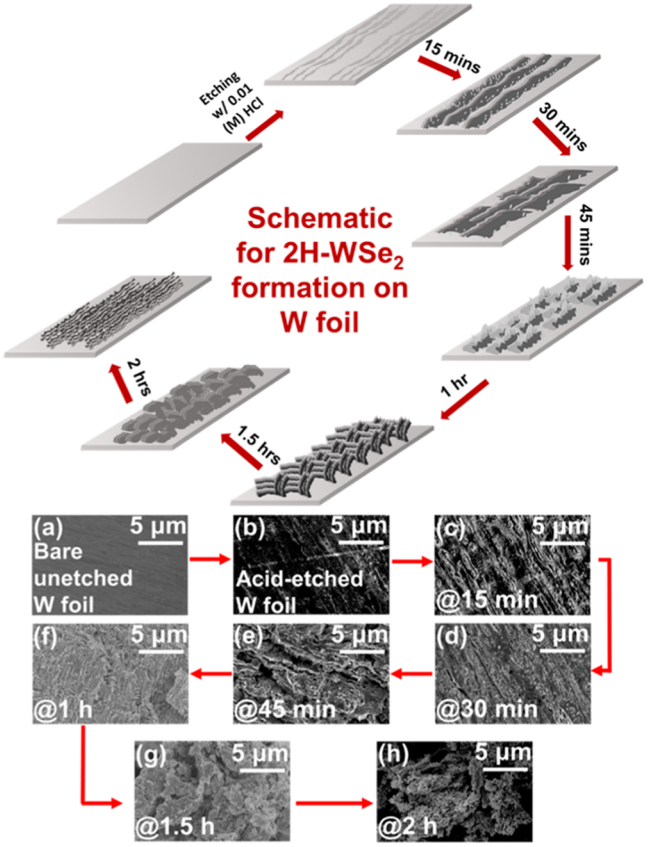

Figure 4. Reaction schematic for growth of 2H-WSe_2 nanoplates on the surface of W foil because of the selenization reaction starting from (a) bare W foil and (b) acid-etched foil to the progression of reaction at W foil surface at (c) 15 min, (d) 30 min, (e) 45 min, (f) 1 h, (g) 1.5 h, and (h) 2 h.

shows striations, which are even more accentuated after acid etching. Since after growth, we also observe striations, we infer that these striations are the initial nucleation sites for the reaction between W and Se to form 2H-WSe_2. The reaction yield increases with time, with a burst after 15 min reaction time, which saturates beyond 1 h (Figure S2 in the Supporting Information). The yield curve appears as an S-curve, which is very typical of coarsening. We also observe that with increasing reaction time, the morphology shows more layers, with the best result after 1 h. However, for too long reaction times (above 1 h), we start losing the layered morphology with the formation of agglomerated areas. After 2 h, we observe the formation of a fluffy powderlike material (as observed while physically handling the bulk material), indicating that the reaction was already complete and that further heat treatment led to weaker adhesion among the individual sheets. This characteristic is also observed while preparing dispersions from the bulk material formed after the 2 h reaction, which led to easier exfoliation of the individual layers. Additionally, after 15 min, we observe many small spherical nanosized structures, which appear to increase in size until 45 min reaction time, which could indicate a secondary growth.

The presence of both W and Se in the bulk 2H-WSe_2 was further qualitatively established from elemental maps obtained using energy-dispersive spectroscopy (EDS). The mapping data were obtained for a small area in a bulk sample of WSe_2, and it exhibited a W/Se ratio very close to 1:2. The overlapped maps for W and Se also indicated a uniform and complete coverage of the W foil with 2H-WSe_2 formation after reacting with elemental selenium. We estimated the amount/yield of 2H-WSe_2 obtained from the liquid exfoliation of the bulk samples. From a 2 cm × 2 cm W foil covered with 2H-WSe_2 in 10 mL of ethanol solution, the yields after drying the ethanol dispersions for each reaction time were: (a) @15 min ∼ 2 mg, (b) @ 30 min ∼ 2.5 mg, (c) @45 min ∼ 4 mg, (d) @1 h ∼ 20 mg, (e) @ 1.5 h ∼ 20.3 mg, and (f) @ 2 h ∼ 20.5 mg (Supporting Figure S2). We, therefore, observe that an increase in reaction time leads to an increase in the yield of the exfoliated material from the bulk 2H-WSe_2, with a significant increase in the yield at 1 h reaction time. Since there was no pronounced increase in the yield after 1 h, we can safely assume that the reaction was already complete.

The depth of the 2H-WSe_2 formed on W foil is estimated using FIB-SEM to be around 5−8 μm (synthesized at 1 h reaction time between W foil and elemental Se (Figure 7a,b8)). The solid-state indirect band gap measurement of the bulk 2H-WSe_2 from the Kubelka−Mulk function is calculated to be around 1.37 eV, which is in agreement with the value of 1.3 eV reported for bulk 2H-WSe_2 in the literature.[41,44,45]

Since the evolution in morphology was most pronounced in the reaction at 1 h (after which the reaction probably saturates, as we mentioned before), we decided to proceed further with this particular reaction set for further analysis using atomic force microscopy (AFM). The bulk tungsten diselenide (2H-WSe_2) samples were prepared for atomic force microscopy (AFM) measurements to see if the material had layers, using a liquid exfoliation technique, where a tiny amount from the bulk 2H-WSe_2 was taken into an appropriate solvent and sonicated in a bath for 60 min until the individual flakes were completely detached from each other and formed a homogeneous dispersion (using 80 kHz and 100% power on the sonicator). A single drop of this ethanol dispersion on a Si/SiO_2 wafer was left to dry for 24 h, and then the portion of the 2H-WSe_2 that was left on the Si/SiO_2 wafer was examined by AFM. For our case, we used three different solvents (ethanol, isopropanol, and hexane) to find which was most appropriate. Only ethanol and isopropanol proved to be the ideal solvents in our liquid exfoliation experiments because hexane degraded our as-synthesized material to some extent. Theoretically, a monolayer should be obtained if the solvent is suitable for exfoliation. Still, we found that we could only exfoliate the bulk material to two layers in both ethanol and isopropanol. A comparison of both the bulk 2H-WSe_2 and exfoliated 2H-WSe_2 (keeping bare W foil as a reference) was made, which helped to identify the difference in the surface microstructure and exfoliated microstructure of the as-synthesized material. The terraces or the steps in the AFM image of bulk WSe_2 were found to be tens of nanometers thick, and the as-grown material is still too thick to point out the monolayers/bilayers correctly. The step-size profile in Figure 5b indicates that the material we prepared was layered, and it was composed of both bigger and smaller flakes/sheets. The stacking of each of the layers is visible. Since the HRSEM measurements also specify that the individual sheets of 2H-WSe_2 are arranged on top of each other, the AFM measurements help to identify the individual heights and also the distribution of the layers in the exfoliated sample. The deposited sheets of WSe_2 on the Si/SiO_2 substrate have different thicknesses and heights, mainly being bilayers and few layers. The bilayer heights or step sizes range around 1.7 ± 0.3 nm. The few-layer step sizes, as observed from Figure 5c, are almost around 4 ± 0.3 nm,

https://dx.doi.org/10.1021/acsomega.0c01155
ACS Omega 2020, 5, 19409−19421

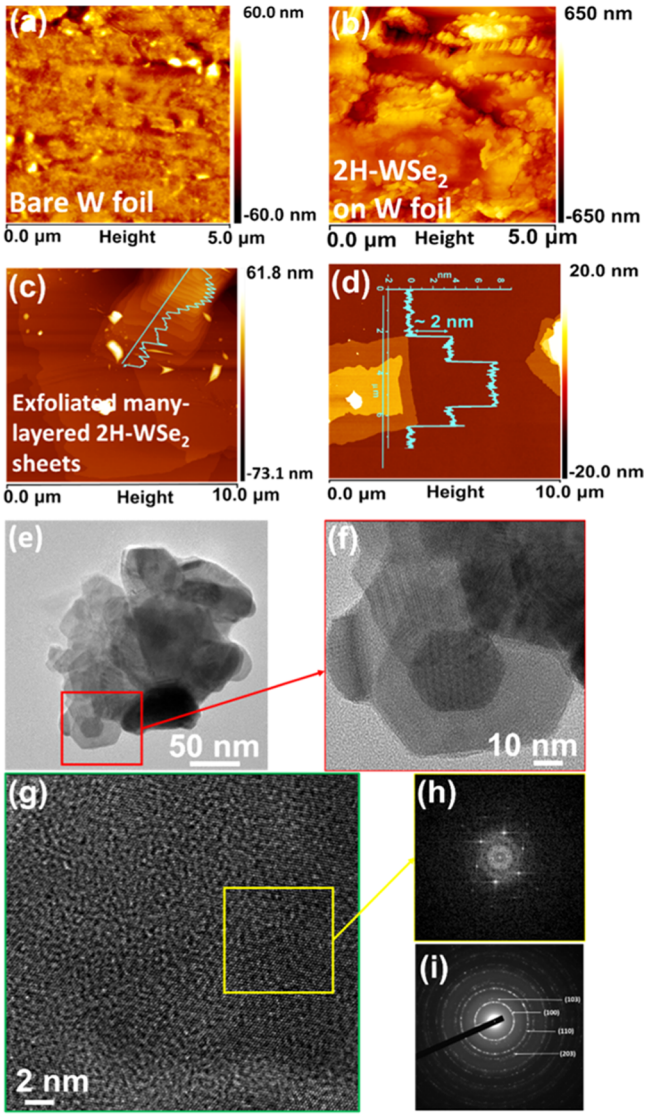

Figure 5. (a–d) AFM images of bare W foil, bulk WSe_2, exfoliated many-layered WSe_2, and exfoliated bilayer WSe_2, respectively; (e–f) BF-TEM images of 2H-WSe_2 with fast Fourier transform (FFT); (g) HRTEM image of 2H-WSe_2 grown at 1 h; (h) FFT image of the highlighted portion in HRTEM; and (i) indexed selected-area electron diffraction (SAED) pattern of 2H-WSe_2 grown at 1 h.

indicating the homogeneous distribution of the exfoliated sample and the presence of almost four to five layers thick material. The lateral thicknesses of the bilayers are estimated to be around 2–3 μm, while the other larger flakes have lateral thicknesses ranging around 4 μm. The results of the AFM measurements are in agreement with the values reported in the literature because the 2H variant of any transition-metal dichalcogenide indicates that the minimum number of layers that might be present after chemical/physical exfoliation is 2.

From the AFM and XRD images of the bulk and the exfoliated 2H-WSe_2 sample, we get an idea that the sample might be layered, two-dimensional, or contain some degree of anisotropy. To endorse our claims, we prepared similar dispersions of 2H-WSe_2 by sonicating at 80 kHz and 100% power for 60 min until we obtained a homogeneous dispersion of the material in the solvent. The solution was then centrifuged, and we took a small amount of this dispersion from the supernatant of the resulting solution and placed it on a copper grid (mesh 300). This solution was dried and observed under a transmission electron microscope (TEM) to identify its characteristic properties. The low-magnification TEM image in Figure 5f gives an idea as to how the exfoliated material looks like when deposited on the copper grid and/or if they are disintegrated on sonication. A closer inspection of the nanosheets revealed that there are distinct layers in the material we synthesized and that each of the layers has almost identical platelike shapes. The portions of the agglomerates, as observed under the TEM, also showed how the individual flakes in the exfoliated 2H-WSe_2 are stacked on top of each other, helping to confirm the findings of the HRSEM imaging and the AFM microscopy results. The length of the nanosheets was also estimated to be around 50–80 nm. The thinnest portions of the material, as observed in the HRTEM bright-field (BF) imaging, could be speculated as a single layer. However, in our case, the presence of bilayers and multilayers (5L) is more prevalent. The high-resolution transmission electron microscopy (HRTEM) measurements help us to identify the SAED pattern (Figure 5i) and calculate the lattice fringes. The (100), (101), (103), and (006) planes were recognized and calculated from the fringes in this particular case. The HRTEM images also help to identify the characteristic honeycomb-like lattice, which is very consistent with the formation of the thermodynamically stable 2H phase of WSe_2. Due to the absence of any other phase of WSe_2 in the HRTEM measurements, it confirms that the material we prepared is indeed phase-pure, whereby all of the peaks obtained in the XRD measurements could be easily correlated. Besides, the high-magnification images (@1 nm) of the HRTEM measurements at different reaction times (15 min (beginning), 1 h (optimized), and 2 h (end)) showed the typical honeycomb arrangement of W and Se throughout the exfoliated samples of 2H-WSe_2. The high-magnification HRTEM images are shown in Figure 6i–iii. In our case, it

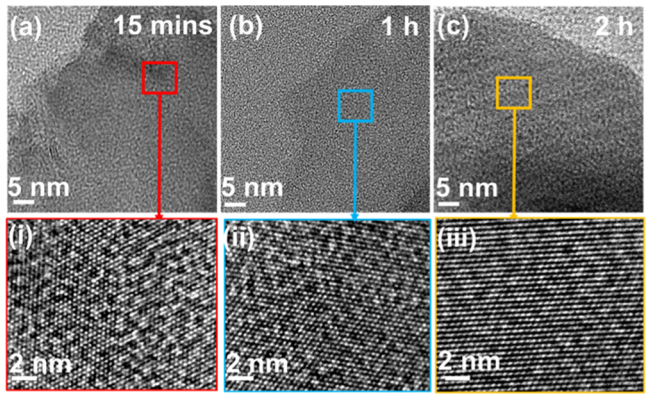

Figure 6. HRTEM image of 2H-WSe_2 at different reaction times in Ar: (a) 15 min, (b) 1 h, and (c) 2 h; (i–iii) high-magnification HRTEM images of (a–c) at three different reaction times (beginning @15 min, optimized @1 h, and prolonged reaction @ 2 h, respectively).

seems that mostly Se vacancies are present, but this is qualitative information based on the EDS measurements obtained from the HRTEM (where W/Se ~ 37:62), which can be explained from a previous report.[46] The d-values calculated from the lattice fringes and FFT patterns of the HRTEM images are slightly deviated compared to the original values in the ICDD reference. Further, HRTEM measurements

https://dx.doi.org/10.1021/acsomega.0c01155
ACS Omega 2020, 5, 19409–19421

of the 2H-WSe_2 samples synthesized in the helium atmosphere at 1.5 and 2 h reaction times (because in He only the more prolonged reaction times were responsive) were also analyzed. They showed similar fast Fourier transforms (FFTs) as the samples synthesized in the Ar atmosphere (Figure S3). We performed a Raman analysis of the exfoliated tungsten diselenide (formed at a 1 h reaction between W foil and elemental Se in Ar). The principle bands were observed at 180 cm^{-1}, and a double peak was observed around 248−256 cm^{-1}; these bands correspond to the frequencies of the Raman-active A_g^1, E_{2g}^1, and, E_{1g} modes of the 2H-WSe_2 crystal structure, which is in correlation with some previous works.[47,48] The absence of the B_{2g}^1 peak at 304 cm^{-1} is an indicator that the flakes of 2H-WSe_2 obtained are 3L−4L. The UV−visible absorption spectra of the WSe_2 show the expected two typical characteristic absorption peaks in the region around 475−800 nm, which correspond to the A1 and B1 direct excitonic transitions of the 2H-WSe_2 originated from the energy split of valence−band and spin−orbital coupling.[49] These two peaks also additionally indicate that WSe_2 was dispersed in ethanol only as of the 2H variant because the excitonic transitions are characteristic of the 2H phase of WSe_2 (Figures 7 and 8).[44]

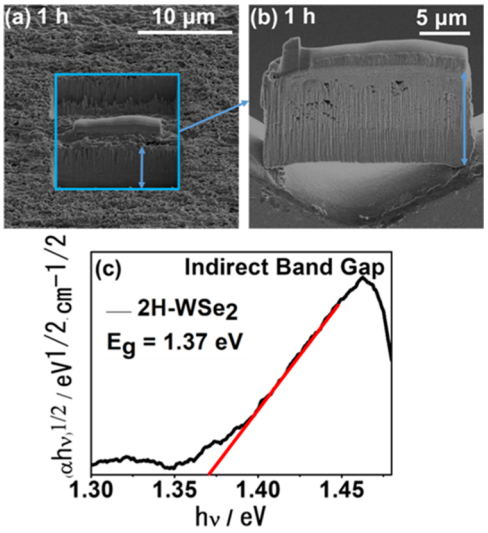

Figure 7. (a, b) FIB-SEM of a lamella of 2H-WSe_2 grown at 1 h reaction between W foil and elemental Se estimating the depth of 2H-WSe_2 growing on W foil; (c) indirect band gap of bulk 2H-WSe_2 synthesized at 1 h reaction between W foil and elemental Se.

So, all of the aforementioned analyses are found to be consistent with the formation of the thermodynamically favorable phase-pure 2H crystal structure of WSe_2 on the W foil, and all of the characterizations of the material enabled us to check it further for application as possible electrode material in lithium-ion battery.

Electrochemical Characterization. The theoretical capacity of WSe_2 is about 313.7 mAh/g based on the following conversion reaction[15]

$$WSe_2 + 4Li^+ + 4e^- \leftrightarrow W + 2Li_2Se \quad (1)$$

When WSe_2 is utilized as a LiB electrode, a voltage window of 0.01−3.0 V is generally used for test.[42] To understand if our material had prospect as electrode material in LiB, the redox processes of the as-synthesized 2H-WSe_2 at 1 h reaction between W foil and elemental Se as precursor and cyclic

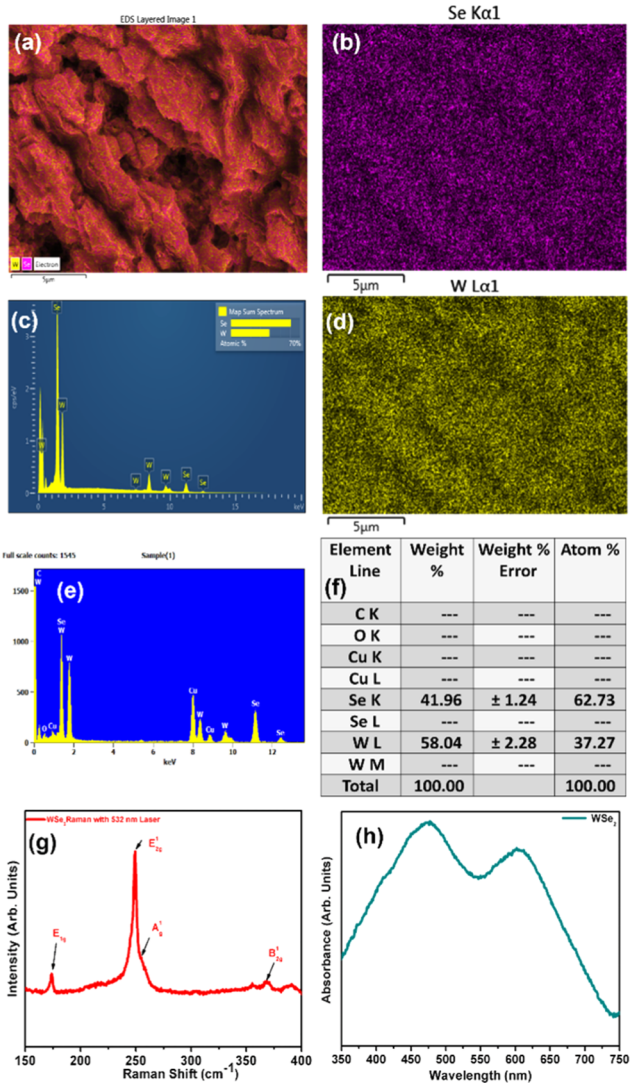

Element Line (f)	Weight %	Weight % Error	Atom %
C K	---	---	---
O K	---	---	---
Cu K	---	---	---
Cu L	---	---	---
Se K	41.96	± 1.24	62.73
Se L	---	---	---
W L	58.04	± 2.28	37.27
W M	---	---	---
Total	100.00		100.00

Figure 8. (a, b) Layered elemental map and energy-dispersive X-ray spectroscopy (EDX), respectively, of bulk 2H-WSe_2; (c, d) elemental mapping of bulk 2H-WSe_2; (e, f) EDS spectra of exfoliated 2H-WSe_2 as obtained from flakes of 2H-WSe_2; (g) UV−vis spectrum of exfoliated 2H-WSe_2; and (h) Raman spectrum of exfoliated 2H-WSe_2.

voltammetry (CV) measurements are tested. The cyclic voltammograms corresponding to the first two cycles at a scan rate of 0.1 mV/s over a potential window of 0.01 V−3.0 V (vs Li/Li^+) are shown in Figure 9a. The voltammogram for the first cycle mainly exhibits a sharp reduction peak at around 0.77 V followed by an oxidation peak at 2.2 V. The reduction peak observed around 0.77 V during the first scan is attributed to the initial conversion of WSe_2 to metallic tungsten and lithium selenide according to eq 1 mentioned above besides the formation of a solid electrolyte interphase on the electrode surface. A careful analysis of the first reduction scan shows multiple reduction peaks at 1.7, 1.54, and 1.37 V (Figure 9a, inset). The appearance of these peaks is associated with the formation of the Li_XWSe_2 phase according to the following equations

$$WSe_2 + xLi^+ + xe^- \rightarrow Li_xWSe_2 \quad (2)$$

$$Li_xWSe_2 + (4 - x)Li^+ + (4 - x)e^- \leftrightarrow W + 2Li_2Se \quad (3)$$

https://dx.doi.org/10.1021/acsomega.0c01155
ACS Omega 2020, 5, 19409−19421

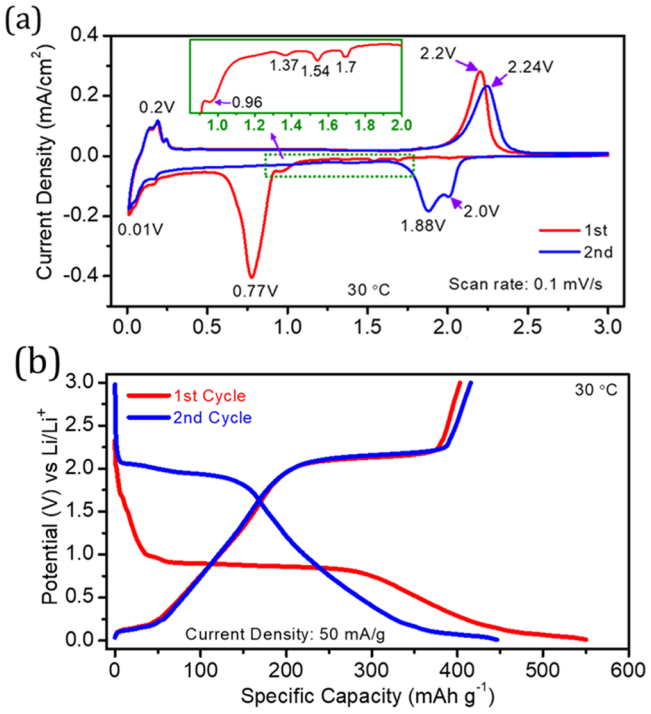

Figure 9. (a) Cyclic voltammograms for the first two cycles of 2H-WSe_2 vs Li at a scan rate of 0.1 mV/s over a potential window of 0.01−3.0 V. (b) Galvanostatic voltage profiles for the first two cycles of WSe_2 in a half-cell recorded at a current density of 50 mA/g.

Here, we propose a stepwise formation of the Li_XWSe_2 phase that occurs within the potential window of 1.8−1.3 V during the first discharge. The occurrence of these multiple peaks, which corroborated to the formation of the Li_XWSe_2 phase, maybe because of the variable electrochemical environment present within the material. To understand the conversion mechanism, we performed an ex situ XRD study of the working electrode at two different discharge states, 0.5 and 0.01 V (vs Li/Li^+). The results are presented in Figure S6. Two as-assembled cells consisting of WSe_2 as the working electrode were discharged to different potentials of 0.5 and 0.01 V (vs Li/Li^+), and X-ray diffractograms were taken from the respective electrodes after dismantling the cells. Figure S6 shows that the intensities of all of the 2H-WSe_2 diffraction peaks diminish gradually, while a new peak at ∼25.8° emerged in the diffraction patterns of the discharged electrode. This new peak ($2\theta \sim 25.8°$) is corroborated to a newly formed Li_2Se phase (JCPDS card no. 65−2985). Since no phases related to Li_xWSe_2 can be seen in our samples, we propose that it exists as an intermediate state, which undergoes final conversion to Li_2Se following eq 3. Furthermore, diffraction peaks of metallic tungsten (W^0) were not found in the sample discharged to 0.01 V, which might be attributed to the poor crystallinity of the W resulted after the conversion.[15]

The CV profile for the second cycle shows two broad cathodic peaks at 1.88 and 2.0 V coupled with a sharp anodic peak at 2.24 V. This redox couple corresponds to the reversible lithiation of WSe_2 to form Li_xWSe_2/Li_2Se and its conversion back to the WSe_2 at 2.24 V during the anodic scan. Furthermore, the weak cathodic and anodic peaks at 0.01 and 0.20 V, respectively, are associated with the intercalation and deintercalation of a minor quantity of Li ions into the electrode material.[50,51] From both the voltammograms, the reversible redox processes of 2H-WSe_2 and its ability to reversibly host Li^+ can be inferred, and we carried out detailed electrochemical investigations. The galvanostatic charge−discharge profile for the first two cycles at a current density of 50 mA/g is presented in Figure 9b. During the first cycle, clear plateaus for the lithiation and delithiation are observed at ∼0.86 and 2.1 V, respectively. WSe_2 exhibits an initial charge/discharge capacity of 403/550 mAh/g, demonstrating a significant first irreversible capacity for solid electrolyte interface formation involving the irreversible consumption of electrolytes on the electrode surface. Here, we observe a specific charge capacity value that is beyond the theoretical capacity [according to eq 1]. This phenomenon is reasonably common for the conversion-type electrodes because of the two crucial facts: (i) interfacial lithium storage through the kinetic activation of the electrode materials[52] and (ii) a partial reversible conversion of the electrode material, which can be coupled with the conductive carbonaceous matrix via a synergistic effect that can perform as the local source for additional Li storage.[53] After the first cycle, lithiation and delithiation are seen at 1.95 and 2.1 V, respectively, which are in good agreement with the peaks observed during the cyclic voltammetry. The proximity of the lithiation and delithiation potentials of WSe_2 further confirms the involvement of the reversible redox process in the charge storage mechanism. Also, a decrease of 100 mAh/g in the specific capacity is observed from the first to the second cycle, which then stabilizes to ∼450 mAh/g. The electrochemical performance as a function of the increasing current densities is then investigated to understand the rate performance of the synthesized 2H-WSe_2. Figure 10 represents the rate perform-

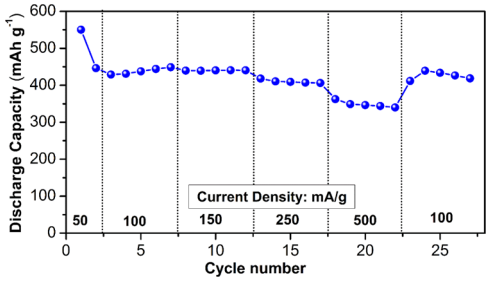

Figure 10. Variation of the discharge capacity as a function of the applied current density measured using 2H-WSe_2 vs Li half-cell.

ance of the 2H-WSe_2. As can be seen from the figure, the specific discharge capacity decreases from 446 (2nd cycle) to 438 (5th cycle), 440 (10th cycle), 409 (15th cycle), and 347 mAh/g (20th cycle) when the current density was increased from 50 to 100, 150, 250, and 500 mA/g, respectively. Additionally, discharge capacities of ∼340 and ∼280 mAh/g were obtained at high current densities of 1000 and 1500 mA/g, respectively (Figure S7). A reversible discharge capacity of 434 mAh/g (25th cycle) is obtained when the current density is decreased to 100 mA/g. Comparing the discharge capacity of 438 mAh/g at the same current density in the fifth cycle, 2H-WSe_2 exhibits a capacity loss of only 0.91%. It can be assumed that the superior electrochemical performance of our material is due to its 2D layered structure, which facilitated the diffusion and storage of Li^+ in the WSe_2 matrix. Next, the cycling stability of the material was investigated. In the initial cycles, a gradual decrease in the discharge capacity was witnessed, which can be attributed to the structural

https://dx.doi.org/10.1021/acsomega.0c01155
ACS Omega 2020, 5, 19409−19421

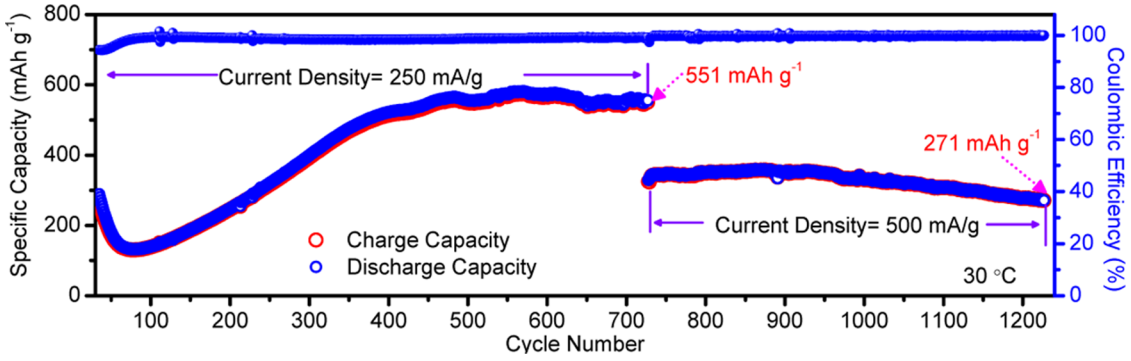

Figure 11. Prolonged electrochemical cycling performance of 2H-WSe_2 electrode in half coin cell configuration (vs Li/Li^+). After the initial 27 cycles of rate performance, the cells were subjected to long-term cycling for 700 cycles at 250 mAh/g and another 500 cycles at 500 mAh/g.

reorganization, volume expansion, as well as sluggish electrolyte penetration into the porous material, resulting in poor wettability during the initial cycles.[54,55] Interestingly, after 50 cycles, a gradual increase in the capacity is seen till 400 cycles, after which capacity was found to be stabilized at ~555 mAh/g at a current density of 250 mA/g till 700 cycles (Figure 11). The increase in capacity after 50 cycles can be linked to additional contribution from the interfacial/surface Li^+ storage mechanism through the kinetic activation of electrode material and accumulation of nanosized conversion residues like W^0 dispersed in layered structures of 2D materials.[56−58] These dispersed redox-active particles in the matrix with a binder and conductive carbon better accommodate the volume changes in addition to shortening the Li^+ diffusion path leading to enhanced capacity.[59,60] A gradual decrease in R_{CT} values observed from the electrochemical impedance spectroscopy (EIS) measurements further supports the aforementioned explanations confirming better charge transfer kinetics of the material after 100 cycles (Figure S8c).

Furthermore, 2H-WSe_2 exhibited a capacity of ~300 mAh/g when the current density was increased to 500 mA/g after ~750 cycles at 250 mA/g. Impressively, even after an additional 500 cycles (total of 1200+ cycles) at 500 mA/g, a capacity of 271 mAh/g with a retention of ~91% was recorded. The observed results for 2H-WSe_2 are quite commendable with the reported results.[22,61−63] The superior rate and stable cycling performance of this electrode material in its pristine form are directly related to the unique morphology. Most importantly, WSe_2 can be a possible conversion electrode material that can substitute the largely studied WS_2-based electrodes because of the significantly reduced overpotential in comparison to WS_2, showing the possibilities for high-energy-efficient devices.[21] The detailed characterization of the phenomenon and further optimization of the material is underway and beyond the scope of this paper, which mainly focuses on the facile and scalable synthesis of 2D layered nanosheets of 2H-WSe_2.

CONCLUSIONS

We reported a facile atmospheric pressure CVD-based synthesis route for synthesizing 2D, layered 2H-WSe_2 in this paper. By carefully studying the process parameters, i.e., the effect of temperature and inert atmospheres, we observed that the material formed at a temperature of 900 °C (at the metal foil side in F2) only in the Ar atmosphere at 1 h reaction between W foil and elemental Se. The phase-pure 2H-WSe_2 we obtained contains a certain degree of anisotropy with some possible defects that need further detailed investigations. We also show a probable reaction mechanism for the growth of 2H-WSe_2 on the W foil, which indicated how surface roughness due to acid etching might have contributed to the formation of 2H-WSe_2. The yield of the exfoliated material we obtained after liquid-based exfoliation of the bulk material (2 cm × 2 cm of W foil on which 2H-WSe_2 has grown) was checked, and it shows an increasing trend (displaying a characteristic S-curve) to increasing time. A significant change in morphology is observed at a 1 h reaction between W foil and Se, leading to the formation of nanoplates/nanosheets. The reaction could also be upscaled easily when we used a W foil of 4 cm x 4 cm cross section using the same optimized process parameters. The bulk and exfoliated material after thorough characterization revealed its structural and physical properties. XRD measurements confirmed the formation of a single phase, while HRSEM, HRTEM, Raman, and band gap measurements helped to identify the 2D layered nature of the material. We carried out electrochemical investigations of the material (optimized at 1 h reaction time) building on its layered structure with a tuned interlayer distance and the ability of 2H-WSe_2 to host the Li^+ to act as a possible electrode material for LiB. Our exfoliated material shows a reversible capacity of 446 mAh/g with appreciable stability and rate performance, signifying its possible application as an electrode material for LiB. Overall, 2H-WSe_2 alone can work as a possible LiB electrode. Further modifications are required related to its structure as well as in-depth study of intermediates formed during prolonged cycling, which are beyond the scope of this paper as it investigates this layered 2D material more from a synthetic point of view.

EXPERIMENTAL SECTION

Synthesis of 2H-WSe_2. The reagents used in our synthesis are of analytical grade and are used in all experiments without further purification. We synthesized tungsten diselenide (WSe_2) using an atmospheric pressure chemical vapor deposition (APCVD), composed of two furnaces (Lindberg Blue) located under a fume hood. The furnaces were equipped with a fused silica (quartz) tube, while the temperatures of the furnaces were monitored using built-in furnace thermocouples. During the growth of WSe_2, the temperatures were set at 650 °C for the first furnace (F1) for elemental Se and 900 °C for the W foil at the second furnace (F2). Argon gas flow (99.9999%, from Gas Technologies) was maintained using electronic mass flows MKS GM50A and controller MKS 946. The synthetic procedure is as follows: We placed a quartz boat

https://dx.doi.org/10.1021/acsomega.0c01155
ACS Omega 2020, 5, 19409−19421

with 1 g of selenium powder (Alfa Aesar, 99.999%) outside of the furnace F1, upstream of the gas flow, and a second quartz boat with two 2 cm × 2 cm pieces of cleaned tungsten (W) foil (Alfa Aesar, 99.999%) downstream, also outside the heated portion of the furnace F2. One of the W foils was cleaned before selenization with 0.01 (M) hydrochloric acid and isopropanol, while the other was cleaned with isopropanol only. After purging the quartz tube with argon for 30 min keeping both boats at room temperature until the furnaces reached equilibrium at the selected temperatures in them, we proceeded to start our experiment. For the growth of tungsten diselenide, we pushed the quartz tube inside the furnace to position the W foil in the middle of the furnace F2 (900 °C). We then introduced the selenium boat at the edge of the first furnace F1 and then slowly pushed it inside the heated area of furnace F1 (set at 650 °C) using an external magnet. At the end of the reaction, we first pulled out the selenium boat from F1. We allowed the as-synthesized material at F2 to stay inside the furnace until it reached room temperature (we turned off the heat of both furnaces), under a constant flow of argon, before removing it from the furnace and exposing it to air. Note that we used the "fast heat technique" according to the thermal annealing reported in our previous papers,[64] but performed a slow cooling of our sample to room temperature while it was still inside the furnace. We also synthesized our material in a two-furnace system rather than a three-zone furnace, which we described during our earlier reports.[65] When we took out the final product from the furnace, we observed a dull gray coating covering the upper exposed surface of the W foil. We refined the process parameters further by varying the growth times of tungsten diselenide (WSe_2) at 1 min, 5 min, 15 min, 30 min, 45 min, 1 h, 1.5 h, and 2 h. We also tested lower growth temperatures of 600, 650, 700, 750, 800, and 850 °C, but none of them showed any observable growth on the surface of the tungsten (W) foil (the details being explained further in the Results and Discussion section). Similar experiments were carried out for another two sets of 4 cm × 4 cm pieces of W foil to check the scalability to the optimized reaction parameters.

Exfoliation of Bulk Tungsten Diselenide (2H-WSe_2). The as-prepared bulk tungsten diselenide (2H-WSe_2) material was exfoliated into few-layer nanosheets using the liquid-phase exfoliation (LPE) method. Typically, the bulk samples were dispersed in ethanol (10 mL, Romical). The dispersions were sonicated continuously for 60 min (optimized for obtaining maximum yield from the bulk material) at room temperature using an ultrasonic bath (Elmasonic P) at a frequency of 80 kHz and power output of 100 W. The dispersions were utilized in subsequent characterizations and dried separately for further usage as a powder material for LiB electrode.

Characterization. *Physical Characterizations.* The X-ray diffraction measurements of the bulk tungsten diselenide (WSe_2) on tungsten (W) foil were performed using a Rigaku SmartLab X-ray diffractometer. We analyzed a 2 cm × 2 cm square sample of bulk tungsten diselenide (WSe_2). The data were collected in the 2θ range of 10−80°, with a step size of 0.004° and a scanning rate of 0.4°/min. The X-ray generator was operated at 40 kV and 30 mA with Cu Kα radiation (λ = 1.542 Å). The crystallinity and purity of the as-synthesized tungsten diselenide (WSe_2) on tungsten (W) foil was further analyzed by X'Pert HighScore Plus software, and the corresponding peaks in the XRD were identified. High-resolution scanning electron microscopy (HRSEM) of the bulk material was carried out using the instrument Magellan 400 FEI for further examination. We performed additional examinations with atomic force microscopy (AFM) measurements. This was done using a Bio Fast Scan scanning probe microscope (Bruker AXS). All images were obtained using tapping mode with a FastScan-A (Bruker) silicon probe (spring constant of 18 N/m). The resonance frequency of the cantilever was approximately 1400 kHz (in air). The measurements were performed under environmental conditions. The images were captured in the retrace direction with a scan rate of 2.0 Hz. The resolution of the images was 512 samples/line. For image processing, Nanoscope Analysis software was used. Before the analysis of the images, the "flatting" and "planefit" functions were applied to each image. We carried out HRTEM analysis of the sample in a JEOL JEM 2100 (operating at 200 keV). We used focused ion beam (FIB) using a Helios 600 FEI to estimate the depth of the 2H-WSe_2 formed on W foil. UV−vis measurements were done in the range of 280−900 nm for 10 mL of the sample in a quartz cell using a Cary 100 spectrophotometer (Varian), operated by LabSphere software. Raman measurements were done using a Thermo Scientific iXR Raman spectrometer. The bulk band gap measurements were done using a Bruker Vertex 70 FT-IR spectrophotometer in DRIFT mode.

Electrochemical Characterizations. Testing of the electrochemical performance of our exfoliated material (2H-WSe_2) is done by fabricating two-electrode coin-type cells. We used a slurry casting method and a standard doctor blade to prepare the working electrodes on a Cu-foil substrate (15 μm thick). A 70:10:10:10 wt % slurry composition mixture containing the electroactive material (2H-WSe_2) (70 wt %), Super C65 carbon (10 wt %), Graphite KS6[66] (10 wt %), and poly(vinylidene fluoride) (10 wt %) in *N*-methyl-2 pyrrolidone was prepared. The cast film (green thickness, 100 mm) kept at 110 °C for 6 h in a vacuum oven vaporized the solvent, and after calendaring at 80 °C in a roller press, it was cut into circular disks of 14 mm diameter. The typical active material loading in these circular electrodes was 1.2−1.4 mg. For coin cell assembly, Li metal was the counter electrode as well as the reference electrode, Celgard 2500 was the separator, and $LiPF_6$ in EC/EMC (3:7 vol%; LP57) was the electrolyte. Cell fabrication was performed inside an argon-filled glovebox keeping the H_2O and O_2 levels at <0.5 ppm. Electrochemical properties were evaluated via cyclic voltammetry (CV) and galvanostatic charge−discharge (GCD) measurements. CV was performed using a VSP potentiostat (BioLogic Science Instruments) in the potential window of 0.01−3.0 V at a scan rate of 0.1 mV/s.

■ ASSOCIATED CONTENT

Supporting Information

The Supporting Information is available free of charge at https://pubs.acs.org/doi/10.1021/acsomega.0c01155.

HRSEM images of 2H-WSe_2 grown in the helium atmosphere (Figure S1); estimated particle size and the optimization of yield from bulk as well as the optimization of the exfoliation time (Figure S2); TEM/HRTEM imaging to determine the d-values of 2H-WSe_2 synthesized in helium atmosphere (Figure S3); elemental mapping, EDS spectra, and HRTEM (FFT image) of postannealed 2H-WSe_2 in Ar (Figure S4); HRSEM imaging of the electrode after 70 cycles

https://dx.doi.org/10.1021/acsomega.0c01155
ACS Omega 2020, 5, 19409−19421

and 127 cycles (Figure S5); X-ray diffraction patterns of 2H-WSe_2 electrodes (performed ex situ) at different states of discharge 0.5 and 0.01 V (vs Li/Li^+) with respect to pristine 2H-WSe_2 electrode shown for comparative understanding (Figure S6); variation of the discharge capacity as a function of applied current density measured in a Li half-cell (Figure S7); and impedance spectra of 2H-WSe_2 as-assembled, after the first formation cycle and after 127 cycles (Figure S8) (PDF)

AUTHOR INFORMATION

Corresponding Authors

Malachi Noked − *Chemistry, Institute of Nanotechnology and Advanced Materials, Bar-Ilan University, Ramat Gan 52900, Israel;* orcid.org/0000-0001-8995-0632; Phone: +972-373-84238; Email: malachi.noked@biu.ac.il

Gilbert Daniel Nessim − *Chemistry, Institute of Nanotechnology and Advanced Materials, Bar-Ilan University, Ramat Gan 52900, Israel;* orcid.org/0000-0003-0738-5436; Phone: +972-373-84540; Email: gilbert.nessim@biu.ac.il

Authors

Rajashree Konar − *Chemistry, Institute of Nanotechnology and Advanced Materials, Bar-Ilan University, Ramat Gan 52900, Israel;* orcid.org/0000-0003-2938-5541

Rosy − *Chemistry, Institute of Nanotechnology and Advanced Materials, Bar-Ilan University, Ramat Gan 52900, Israel;* orcid.org/0000-0001-5985-8587

Ilana Perelshtein − *Institute of Nanotechnology and Advanced Materials, Bar-Ilan University, Ramat Gan 52900, Israel*

Eti Teblum − *Institute of Nanotechnology and Advanced Materials, Bar-Ilan University, Ramat Gan 52900, Israel*

Madina Telkhozhayeva − *Chemistry, Institute of Nanotechnology and Advanced Materials, Bar-Ilan University, Ramat Gan 52900, Israel*

Maria Tkachev − *Institute of Nanotechnology and Advanced Materials, Bar-Ilan University, Ramat Gan 52900, Israel*

Jonathan J. Richter − *Chemistry, Institute of Nanotechnology and Advanced Materials, Bar-Ilan University, Ramat Gan 52900, Israel*

Elti Cattaruzza − *Department of Molecular Sciences and Nanosystems, Ca'Foscari University of Venice, Venezia-Mestre 30172, Italy;* orcid.org/0000-0003-0643-0266

Andrea Pietropolli Charmet − *Department of Molecular Sciences and Nanosystems, Ca'Foscari University of Venice, Venezia-Mestre 30172, Italy;* orcid.org/0000-0002-1490-5754

Paolo Stoppa − *Department of Molecular Sciences and Nanosystems, Ca'Foscari University of Venice, Venezia-Mestre 30172, Italy*

Complete contact information is available at: https://pubs.acs.org/10.1021/acsomega.0c01155

Notes

The authors declare no competing financial interest.

ACKNOWLEDGMENTS

G.D.N. is thankful to the Israel Science Foundation and Israel Prime Ministry Office for alternatives initiative for partial funding of this study under the Israel Research center for Electrochemical Propulsion (INREP) (Grant: ISF 2797/11) and European Union's Horizon 2020 research and innovation program under grant agreement no. 814413, project ADMAIORA. Madina Telkhozhayeva is thankful to Erasmus + ICM (ERASMUS + KA107 ICM).

REFERENCES

(1) Chen, F.; Wang, J.; Li, B.; Yao, C.; Bao, H.; Shi, Y. Nanocasting Synthesis of Ordered Mesoporous Crystalline WSe_2 as Anode Material for Li-Ion Batteries. *Mater. Lett.* **2014**, *136*, 191−194.

(2) Han, X.; Lu, L.; Zheng, Y.; Feng, X.; Li, Z.; Li, J.; Ouyang, M. A Review on the Key Issues of the Lithium Ion Battery Degradation among the Whole Life Cycle. *eTransportation* **2019**, *1*, No. 100005.

(3) Santhosha, A. L.; Nayak, P. K.; Pollok, K.; Langenhorst, F.; Adelhelm, P. Exfoliated MoS_2 as Electrode for All-Solid-State Rechargeable Lithium-Ion Batteries. *J. Phys. Chem. C* **2019**, *123*, 12126−12134.

(4) Xia, H.; Xu, Q.; Zhang, J. Recent Progress on Two-Dimensional Nanoflake Ensembles for Energy Storage Applications. *Nano-Micro Lett.* **2018**, *10*, No. 66.

(5) Wu, Y.; Yu, Y. 2D Material as Anode for Sodium Ion Batteries: Recent Progress and Perspectives. *Energy Storage Mater.* **2019**, *16*, 323−343.

(6) Choudhuri, I.; Bhauriyal, P.; Pathak, B. Recent Advances in Graphene-like 2D Materials for Spintronics Applications. *Chem. Mater.* **2019**, *31*, 8260−8285.

(7) Khan, K.; Tareen, A. K.; Aslam, M.; Zhang, Y.; Wang, R.; Ouyang, Z.; Gou, Z.; Zhang, H. Recent Advances in Two-Dimensional Materials and Their Nanocomposites in Sustainable Energy Conversion Applications. *Nanoscale* **2019**, *11*, 21622−21678.

(8) Chhowalla, M.; Shin, H. S.; Eda, G.; Li, L.; Loh, K. P.; Zhang, H. The Chemistry of Two-Dimensional Layered Transition Metal Dichalcogenide Nanosheets. *Nat. Chem.* **2013**, *5*, 263−275.

(9) Nicolosi, V.; Chhowalla, M.; Kanatzidis, M. G.; Strano, M. S.; Coleman, J. N. Liquid Exfoliation of Layered Materials. *Science* **2013**, *340*, 1226419.

(10) Feng, X.; Tang, Q.; Zhou, J.; Fang, J.; Ding, P.; Sun, L.; Shi, L. Novel Mixed-Solvothermal Synthesis of MoS 2 Nanosheets with Controllable Morphologies. *Cryst. Res. Technol.* **2013**, *48*, 363−368.

(11) Ye, G.; Gong, Y.; Lei, S.; He, Y.; Li, B.; Zhang, X.; Jin, Z.; Dong, L.; Lou, J.; Vajtai, R.; Zhou, W.; Ajayan, P. M. Synthesis of Large-Scale Atomic-Layer SnS_2 through Chemical Vapor Deposition. *Nano Res.* **2017**, *10*, 2386−2394.

(12) Shi, L.; Zhao, T. Recent Advances in Inorganic 2D Materials and Their Applications in Lithium and Sodium Batteries. *J. Mater. Chem. A* **2017**, *5*, 3735−3758.

(13) Kim, T.-Y.; Song, Y.; Cho, K.; Amani, M.; Ho Ahn, G.; Kim, J.-K.; Pak, J.; Chung, S.; Javey, A.; Lee, T. Analysis of the Interface Characteristics of CVD-Grown Monolayer MoS 2 by Noise Measurements. *Nanotechnology* **2017**, *28*, No. 145702.

(14) Brent, J. R.; Savjani, N.; O'Brien, P. Synthetic Approaches to Two-Dimensional Transition Metal Dichalcogenide Nanosheets. *Prog. Mater. Sci.* **2017**, *89*, 411−478.

(15) Yang, W.; Wang, J.; Si, C.; Peng, Z.; Zhang, Z. Tungsten Diselenide Nanoplates as Advanced Lithium/Sodium Ion Electrode Materials with Different Storage Mechanisms. *Nano Res.* **2017**, *10*, 2584−2598.

(16) Jariwala, D.; Sangwan, V. K.; Lauhon, L. J.; Marks, T. J.; Hersam, M. C. Emerging Device Applications for Semiconducting Two-Dimensional Transition Metal Dichalcogenides. *ACS Nano* **2014**, *8*, 1102−1120.

(17) Eftekhari, A. Tungsten Dichalcogenides (WS 2, WSe 2, and WTe 2): Materials Chemistry and Applications. *J. Mater. Chem. A* **2017**, *5*, 18299−18325.

(18) Nguyen, D. A.; Oh, H. M.; Duong, N. T.; Bang, S.; Yoon, S. J.; Jeong, M. S. Highly Enhanced Photoresponsivity of a Monolayer WSe 2 Photodetector with Nitrogen-Doped Graphene Quantum Dots. *ACS Appl. Mater. Interfaces* **2018**, *10*, 10322−10329.

(19) Ghosh, S.; Wasala, M.; Pradhan, N. R.; Rhodes, D.; Patil, P. D.; Fralaide, M.; Xin, Y.; McGill, S. A.; Balicas, L.; Talapatra, S. Low Temperature Photoconductivity of Few Layer p-Type Tungsten Diselenide (WSe_2) Field-Effect Transistors (FETs). *Nanotechnology* **2018**, *29*, No. 484002.
(20) Liu, H.; Su, D.; Wang, G.; Qiao, S. Z. An Ordered Mesoporous WS_2 Anode Material with Superior Electrochemical Performance for Lithium Ion Batteries. *J. Mater. Chem.* **2012**, *22*, 17437.
(21) Share, K.; Lewis, J.; Oakes, L.; Carter, R. E.; Cohn, A. P.; Pint, C. L. Tungsten Diselenide (WSe_2) as a High Capacity, Low Overpotential Conversion Electrode for Sodium Ion Batteries. *RSC Adv.* **2015**, *5*, 101262−101267.
(22) Huang, J.; Wei, Z.; Liao, J.; Ni, W.; Wang, C.; Ma, J. Molybdenum and Tungsten Chalcogenides for Lithium/Sodium-Ion Batteries: Beyond MoS2. *J. Energy Chem.* **2019**, *33*, 100−124.
(23) Zhang, Z.; Yang, X.; Fu, Y. Nanostructured WSe_2/C Composites as Anode Materials for Sodium-Ion Batteries. *RSC Adv.* **2016**, *6*, 12726−12729.
(24) Wang, X.; He, J.; Zheng, B.; Zhang, W.; Chen, Y. Few-Layered WSe_2 in-Situ Grown on Graphene Nanosheets as Efficient Anode for Lithium-Ion Batteries. *Electrochim. Acta* **2018**, *283*, 1660−1667.
(25) You, J.; Hossain, M. D.; Luo, Z. Synthesis of 2D Transition Metal Dichalcogenides by Chemical Vapor Deposition with Controlled Layer Number and Morphology. *Nano Converg.* **2018**, *5*, 26.
(26) Yu, J.; Li, J.; Zhang, W.; Chang, H. Synthesis of High Quality Two-Dimensional Materials via Chemical Vapor Deposition. *Chem. Sci.* **2015**, *6*, 6705−6716.
(27) Shinde, S. M.; Kano, E.; Kalita, G.; Takeguchi, M.; Hashimoto, A.; Tanemura, M. Grain Structures of Nitrogen-Doped Graphene Synthesized by Solid Source-Based Chemical Vapor Deposition. *Carbon* **2016**, *96*, 448−453.
(28) Cai, Y.; Xu, K.; Zhu, W. Synthesis of Transition Metal Dichalcogenides and Their Heterostructures. *Mater. Res. Express* **2018**, *5*, No. 095904.
(29) Zhai, T.; Gu, Z.; Ma, Y.; Yang, W.; Zhao, L.; Yao, J. Synthesis of Ordered ZnS Nanotubes by MOCVD-Template Method. *Mater. Chem. Phys.* **2006**, *100*, 281−284.
(30) Eichfeld, S. M.; Hossain, L.; Lin, Y.-C.; Piasecki, A. F.; Kupp, B.; Birdwell, A. G.; Burke, R. A.; Lu, N.; Peng, X.; Li, J.; Azcatl, A.; McDonnell, S.; Wallace, R. M.; Kim, M. J.; Mayer, T. S.; Redwing, J. M.; Robinson, J. M. Highly Scalable, Atomically Thin WSe_2 Grown via Metal−Organic Chemical Vapor Deposition. *ACS Nano* **2015**, *9*, 2080−2087.
(31) Chimupala, Y.; Junploy, P.; Hardcastle, T.; Westwood, A.; Scott, A.; Johnson, B.; Brydson, R. Universal Synthesis Method for Mixed Phase TiO 2 (B)/Anatase TiO 2 Thin Films on Substrates via a Modified Low Pressure Chemical Vapour Deposition (LPCVD) Route. *J. Mater. Chem. A* **2016**, *4*, 5685−5699.
(32) Cao, H.-W.; Zhao, H.-M.; Xin, X.; Shao, P.-Z.; Qi, H.-Y.; Jian, M.-Q.; Zhang, Y.-Y.; Yang, Y.; Ren, T.-L. Large-Scale Synthesis of WSe_2 Atomic Layers on SiO_2 /Si. *Mod. Phys. Lett. B* **2016**, *30*, No. 1650267.
(33) Irisawa, T.; Okada, N.; Mizubayashi, W.; Mori, T.; Chang, W.-H.; Koga, K.; Ando, A.; Endo, K.; Sasaki, S.; Endo, T.; Miyata, Y. CVD Growth Technologies of Layered MX_2 Materials for Real LSI Applications—Position and Growth Direction Control and Gas Source Synthesis. *IEEE J. Electron Devices Soc.* **2018**, *6*, 1159−1163.
(34) Bosi, M. Growth and Synthesis of Mono and Few-Layers Transition Metal Dichalcogenides by Vapour Techniques: A Review. *RSC Adv.* **2015**, *5*, 75500−75518.
(35) Shupp, J. P.; Kinne, A. S.; Arman, H. D.; Tonzetich, Z. J. Synthesis and Characterization of Molybdenum(0) and Tungsten(0) Complexes of Tetramethylthiourea: Single-Source Precursors for MoS 2 and WS 2. *Organometallics* **2014**, *33*, 5238−5245.
(36) Jang, Y. S.; Kang, Y. C. Facile One-Pot Synthesis of Spherical Zinc Sulfide−Carbon Nanocomposite Powders with Superior Electrochemical Properties as Anode Materials for Li-Ion Batteries. *Phys. Chem. Chem. Phys.* **2013**, *15*, 16437.
(37) Li, W.-J.; Fu, Z.-W. Nanostructured WO_3 Thin Film as a New Anode Material for Lithium-Ion Batteries. *Appl. Surf. Sci.* **2010**, *256*, 2447−2452.
(38) Zhou, J.; Li, J.; Liu, K.; Lan, L.; Song, H.; Chen, X. Free-Standing Cobalt Hydroxide Nanoplatelet Array Formed by Growth of Preferential-Orientation on Graphene Nanosheets as Anode Material for Lithium-Ion Batteries. *J. Mater. Chem. A* **2014**, *2*, 20706−20713.
(39) Dutrizac, J. E. The Reaction of Tungsten with Selenium Vapor. *J. Less-Common Met.* **1973**, *33*, 341−353.
(40) Liu, H. J.; Jiao, L.; Xie, L.; Yang, F.; Chen, J. L.; Ho, W. K.; Gao, C. L.; Jia, J. F.; Cui, X. D.; Xie, M. H. Molecular-Beam Epitaxy of Monolayer and Bilayer WSe2: A Scanning Tunneling Microscopy/Spectroscopy Study and Deduction of Exciton Binding Energy. *2D Mater.* **2015**, *2*, No. 034004.
(41) Mao, X.; Zou, J.; Li, H.; Song, Z.; He, S. Magnetron Sputtering Fabrication and Photoelectric Properties of WSe2 Film Solar Cell Device. *Appl. Surf. Sci.* **2018**, *444*, 126−132.
(42) Vishwanath, S.; Liu, X.; Rouvimov, S.; Basile, L.; Lu, N.; Azcatl, A.; Magno, K.; Wallace, R. M.; Kim, M.; Idrobo, J.-C.; Furdyna, J. K.; Jena, D.; Xing, H. G. Controllable Growth of Layered Selenide and Telluride Heterostructures and Superlattices Using Molecular Beam Epitaxy. *J. Mater. Res.* **2016**, *31*, 900−910.
(43) Jakubowicz, A.; Mahalu, D.; Wolf, M.; Wold, A.; Tenne, R. WSe_2: Optical and Electrical Properties as Related to Surface Passivation Of Recombination Centers A. *Phys. Rev. B* **1989**, *40*, 2992−3000.
(44) Coehoorn, R.; Haas, C.; Dijkstra, J.; Flipse, C. J. F.; de Groot, R. A.; Wold, A. E. Electronic Structure of $MoSe_2$, MoS_2, and WSe_2. I. Band-Structure Calculations and Photoelectron Spectroscopy. *Phys. Rev. B* **1987**, *35*, 6195−6202.
(45) Razavi-Khosroshahi, H.; Edalati, K.; Wu, J.; Nakashima, Y.; Arita, M.; Ikoma, Y.; Sadakiyo, M.; Inagaki, Y.; Staykov, A.; Yamauchi, M.; Horita, Z.; Fuji, M. High-Pressure Zinc Oxide Phase as Visible-Light-Active Photocatalyst with Narrow Band Gap. *J. Mater. Chem. A* **2017**, *5*, 20298−20303.
(46) Lin, Y.-C.; Björkman, T.; Komsa, H.-P.; Teng, P.-Y.; Yeh, C.-H.; Huang, F.-S.; Lin, K.-H.; Jadczak, J.; Huang, Y.-S.; Chiu, P.-W.; Krasheninnikov, A. V.; Suenaga, K. Three-Fold Rotational Defects in Two-Dimensional Transition Metal Dichalcogenides. *Nat. Commun.* **2015**, *6*, No. 6736.
(47) Zeng, H.; Liu, G.-B.; Dai, J.; Yan, Y.; Zhu, B.; He, R.; Xie, L.; Xu, S.; Chen, X.; Yao, W.; Cui, X. Optical Signature of Symmetry Variations and Spin-Valley Coupling in Atomically Thin Tungsten Dichalcogenides. *Sci. Rep.* **2013**, *3*, No. 1608.
(48) del Corro, E.; Terrones, H.; Elias, A.; Fantini, C.; Feng, S.; Nguyen, M. A.; Mallouk, T. E.; Terrones, M.; Pimenta, M. A. Excited Excitonic States in 1L, 2L, 3L, and Bulk WSe 2 Observed by Resonant Raman Spectroscopy. *ACS Nano* **2014**, *8*, 9629−9635.
(49) Klots, A. R.; Newaz, A. K. M.; Wang, B.; Prasai, D.; Krzyzanowska, H.; Lin, J.; Caudel, D.; Ghimire, N. J.; Yan, J.; Ivanov, B. L.; Velizhanin, K. A.; Burger, A.; Mandrus, D. G.; Tolk, N. H.; Pantelides, S. T.; Bolotin, K. I. Probing Excitonic States in Suspended Two-Dimensional Semiconductors by Photocurrent Spectroscopy. *Sci. Rep.* **2015**, *4*, No. 6608.
(50) Zeng, L.; Luo, F.; Chen, X.; Xu, L.; Xiong, P.; Feng, X.; Luo, Y.; Chen, Q.; Wei, M.; Qian, Q. An Ultra-Small Few-Layer MoS_2-Hierarchical Porous Carbon Fiber Composite Obtained via Nano-casting Synthesis for Sodium-Ion Battery Anodes with Excellent Long-Term Cycling Performance. *Dalton Trans.* **2019**, *48*, 4149−4156.
(51) Kim, I.; Park, S.-W.; Kim, D.-W. Carbon-Coated Tungsten Diselenide Nanosheets Uniformly Assembled on Porous Carbon Cloth as Flexible Binder-Free Anodes for Sodium-Ion Batteries with Improved Electrochemical Performance. *J. Alloys Compd.* **2020**, *827*, No. 154348.
(52) Chen, K.; Xue, D.; Komarneni, S. Beyond Theoretical Capacity in Cu-Based Integrated Anode: Insight into the Structural Evolution of CuO. *J. Power Sources* **2015**, *275*, 136−143.

https://dx.doi.org/10.1021/acsomega.0c01155
ACS Omega 2020, 5, 19409−19421

(53) Wang, Y.; Huang, Z. X.; Shi, Y.; Wong, J. I.; Ding, M.; Yang, H. Y. Designed Hybrid Nanostructure with Catalytic Effect: Beyond the Theoretical Capacity of SnO2 Anode Material for Lithium Ion Batteries. *Sci. Rep.* **2015**, *5*, No. 9164.
(54) Lou, X. W.; Deng, D.; Lee, J. Y.; Feng, J.; Archer, L. A. Self-Supported Formation of Needlelike Co_3O_4 Nanotubes and Their Application as Lithium-Ion Battery Electrodes. *Adv. Mater.* **2008**, *20*, 258−262.
(55) Ban, C.; Wu, Z.; Gillaspie, D. T.; Chen, L.; Yan, Y.; Blackburn, J. L.; Dillon, A. C. Nanostructured Fe_3O_4/SWNT Electrode: Binder-Free and High-Rate Li-Ion Anode. *Adv. Mater.* **2010**, *22*, E145−E149.
(56) Grugeon, S.; Laruelle, S.; Dupont, L.; Tarascon, J. M. An Update on the Reactivity of Nanoparticles Co-Based Compounds towards Li. *Solid State Sci.* **2003**, *5*, 895−904.
(57) Poizot, P.; Laruelle, S.; Grugeon, S.; Dupont, L.; Tarascon, J. Nano-Sized transition-Metal oxides as Negative-Electrode Materials for Lithium-Ion Batteries. *Nature* **2000**, *407*, 496−499.
(58) Zhou, G.; Wang, D.-W.; Li, F.; Zhang, L.; Li, N.; Wu, Z.-S.; Wen, L.; Lu, G. Q. Max; Cheng, H.-M. Graphene-Wrapped Fe_3O_4 Anode Material with Improved Reversible Capacity and Cyclic Stability for Lithium Ion Batteries. *Chem. Mater.* **2010**, *22*, 5306−5313.
(59) Hu, Y.-S.; Guo, Y.-G.; Dominko, R.; Gaberscek, M.; Jamnik, J.; Maier, J. Improved Electrode Performance of Porous $LiFePO_4$ Using RuO_2 as an Oxidic Nanoscale Interconnect. *Adv. Mater.* **2007**, *19*, 1963−1966.
(60) Armand, M.; Tarascon, J.-M. Building Better Batteries. *Nature* **2008**, *451*, 652−657.
(61) Lee, Y. Y.; Park, G. O.; Choi, Y. S.; Shon, J. K.; Yoon, J.; Kim, K. H.; Yoon, W.-S.; Kim, H.; Kim, J. M. Mesoporous Transition Metal Dichalcogenide ME_2 (M = Mo, W; E = S, Se) with 2-D Layered Crystallinity as Anode Materials for Lithium Ion Batteries. *RSC Adv.* **2016**, *6*, 14253−14260.
(62) Li, J.; Han, S.; Zhang, J.; Xiang, J.; Zhu, X.; Liu, P.; Li, X.; Feng, C.; Xiang, B.; Gu, M. Synthesis of Three-Dimensional Free-Standing WSe_2/C Hybrid Nanofibers as Anodes for High-Capacity Lithium/Sodium Ion Batteries. *J. Mater. Chem. A* **2019**, *7*, 19898−19908.
(63) Wang, J.; Chen, L.; Zeng, L.; Wei, Q.; Wei, M. In Situ Synthesis of WSe_2/CMK-5 Nanocomposite for Rechargeable Lithium-Ion Batteries with a Long-Term Cycling Stability. *ACS Sustainable Chem. Eng.* **2018**, *6*, 4688−4694.
(64) Itzhak, A.; Teblum, E.; Girshevitz, O.; Okashy, S.; Turkulets, Y.; Burlaka, L.; Cohen-Taguri, G.; Shawat Avraham, E.; Noked, M.; Shalish, I.; Nessim, G. D. Digenite (Cu_9S_5): Layered p-Type Semiconductor Grown by Reactive Annealing of Copper. *Chem. Mater.* **2018**, *30*, 2379−2388.
(65) Shokhen, V.; Kostikov, Y.; Borge-Durán, I.; Gershinsky, Y.; Grinberg, I.; Nessim, G. D.; Zitoun, D. Scalable Silver Oxo-Sulfide Catalyst for Electrochemical Water Splitting. *ACS Appl. Energy Mater.* **2019**, *2*, 788−796.
(66) Hong, J. K.; Lee, J. H.; Oh, S. M. Effect of Carbon Additive on Electrochemical Performance of LiCoO2 Composite Cathodes. *J. Power Sources* **2002**, *111*, 90−96.

https://dx.doi.org/10.1021/acsomega.0c01155
ACS Omega 2020, 5, 19409−19421